Heuristic model of Purcell enhancement in photonic crystal waveguides

Alexander Shurinov,[1] Ivan Dyakonov,[1,2,*] Sergei Kulik,[1,3] and Stanislav Straupe[1,2]

[1] *Quantum Technologies Centre, Lomonosov Moscow State University, Leninskie Gory 1 Building 35, Moscow, 119991, Russia*

[2] *Russian Quantum Center, Bol'shoy Bul'var 30 Building 1, Moscow, 121205, Russia*

[3] *Laboratory of Quantum Engineering of Light, South Ural State University, Prospekt Lenina 76, Chelyabinsk, 454080, Russia*

(Received 28 October 2022; revised 9 August 2023; accepted 19 October 2023; published 21 November 2023)

We present a heuristic mathematical model of the relation between the geometry of a photonic crystal waveguide and the Purcell-enhancement factor at a particular wavelength of interest. We use this model to propose approaches to the design of a photonic crystal waveguide maximizing the Purcell enhancement at a target wavelength. Numerical simulations indicate that the proposed model allows controlled variation of Purcell-factor peak width and height, which can be used to achieve increased robustness with regard to fabrication defects.

DOI: 10.1103/PhysRevApplied.20.054044

I. INTRODUCTION

A planar photonic crystal (PC) waveguide (PCW) is a rich system finding applications in diverse areas of optical physics, such as slow light [1], topological photonics [2], chiral photonics [3], and cavity quantum electrodynamics [4]. An attractive feature of the planar photonic crystal is its flexibility for tailoring dispersion properties of light. In particular, the dispersion curve of a PCW mode inside the crystal band gap can be engineered to reach extremely high values of the group velocity at a target wavelength. This feature allows one to use a PCW as a platform for traveling-wave cavity quantum electrodynamics [5,6]. A single emitter generating photons at a frequency ω_d matched to the large group-velocity range of the PCW-mode dispersion curve is strongly coupled to the PCW mode and thus its emission exhibits a significant Purcell enhancement. This effect enabled the development of an on-demand single-photon source compatible with planar photonic integrated circuits [7]. Furthermore, the ability to strongly couple an emitter to a cavity mode while still being able to efficiently excite the emitter and read out photons from the cavity boosted research in nonlinear light-matter interaction at the single-photon level [8].

Semiconductor quantum dots (QDs) are the commonest type of emitter that can be coupled to a PCW to create a single-photon source [7,9]. Despite being well studied, QDs with predefined parameters are still notoriously hard to fabricate deterministically. The widespread Stransky-Krastanov growth process produces QDs with randomly distributed spectral characteristics. The emission wavelength of QDs typically falls in a range of a few teraherz around the designed center frequency. The first derivative $d\omega/dk$ of the PCW dispersion curve becomes close to zero in a very narrow frequency range $\omega_0 \pm \Delta\omega/2$, and efficient Purcell enhancement is not guaranteed for most of the fabricated QDs with emission frequencies missing the $\Delta\omega$ region. Furthermore, the fabrication process introduces defects into the PCW structure that affect the dispersion properties of the PCW mode. The workaround for this issue is straightforward—an array of structures is fabricated and only those that meet particular experimental requirements are selected. Although this method may be satisfactory for research purposes, the lack of reproducibility in the single-photon-source fabrication is one of the major bottlenecks in contemporary quantum optical experiments [10]. At the same time, current trends in optical quantum computing require the development of hybrid integration methods to place single emitters onto a photonic platform of choice [11].

The design of a photonic crystal waveguide for a particular purpose is typically converted into a problem of fine adjustment of dispersion properties of the system. This can be achieved by careful analysis of the photonic crystal geometry [12], by modifying the hole pattern or hole shape [13–16], or even by altering the refractive index of the material within the holes [17]. The methods used to find appropriate configurations use mapping of the parameter space using finite-difference time-domain (FDTD) simulations [12], analysis of the structures in Fourier space [18], or implementation of a numerical optimization routine to adjust the topology on the basis of a defined figure of merit

*dyakonov@quantum.msu.ru

[19–22]. Each of these methods depends on FDTD simulations that might limit applications of PCWs in a broader range of areas.

In this paper we address the task of finding an optimal PCW configuration that maximizes the Purcell enhancement at a given frequency. We start by developing a heuristic PCW design approach that significantly simplifies the selection of a PCW geometric configuration. The theory behind this approach is based on simple optical phenomena—interference and diffraction of light scattered inside the PCW membrane and leaking out of the membrane. The derived equations provide clear guidelines for how to choose PCW geometric parameters so as to set the maximal Purcell enhancement at the required frequency and completely eliminate the necessity to evaluate multiple time-consuming 3D FDTD simulations. A similar effort was reported in Ref. [23]; however, the interplay between the structure parameters has not been described in detail. After the description of the heuristic PCW theory, we address the problem of PCW robustness with regard to fabrication imperfections. The question of PCW-dispersion-curve robustness with regard to fabrication defects has been highlighted in a series of studies. These include studies of the influence of fabrication defects on the quality factors of photonic crystal microcavities [24,25] and automated design methods to optimize the photonic crystal microcavity structure [22,26]. We demonstrate that the proposed theoretical description helps to easily find PCW structures with increased robustness of the coupling between an emitter and a photonic-crystal-waveguide mode. We propose two design approaches for increasing the robustness of coupling with regard to the fabrication errors and test them using numerical simulations.

II. PHOTONIC CRYSTAL

A typical 2D photonic crystal is a periodic arrangement of circular holes etched in a thin film of a material with high refractive index. A deleted row of holes forms a photonic crystal waveguide (see Fig. 1). A characteristic feature of a PCW is the existence of a frequency range where the group velocity of light decreases significantly. This fact makes a PCW structure an extremely appealing system for mediating interaction between light and an isolated dipole. A PCW effectively serves as a microresonator with a small mode volume and a high quality factor. Such systems were demonstrated to suite the purpose of integration of A_3B_5-quantum-dot single-photon sources in a planar photonic structure [7]. A quantum dot can be considered as a dipole, which is oriented perpendicular to the waveguide axis in the PC plane. A PCW microresonator forms an open cavity that can be smoothly interfaced with other integrated photonic waveguides.

We focus our attention on a PCW created by deletion of a row of air holes from a 2D triangular array. The host material is chosen to be gallium arsenide (GaAs) because the target application is a planar semiconductor-quantum-dot single-photon source. We start with the description of the PCW characteristics and development of its heuristic model. Manga Rao and Hughes [27] derived an expression for a Purcell factor F_{PCW} in terms of PCW parameters:

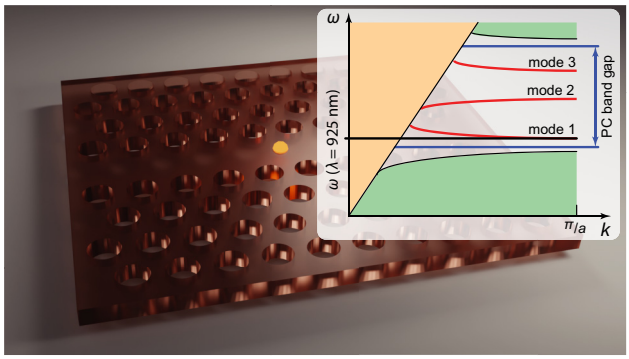

FIG. 1. Overview of a photonic-crystal-waveguide structure. The inset illustrates typical dispersion curves of PCW eigenmodes inside the photonic band gap. The example illustrates the existence of three modes (red lines). Blue lines indicate the PC band gap before hole removal. Green areas indicate PCW bulk modes and the yellow area corresponds to light waves with a nonzero wavevector component orthogonal to the PCW-membrane surface.

$$F_{\mathrm{PCW}} = \frac{3\pi c^3 a}{V_{\mathrm{eff}}\omega_d^2 \epsilon^{3/2} v_g}, \tag{1}$$

where a is the distance between two neighboring air holes assuming the lattice is triangular from now on, V_{eff} is the effective mode volume, and v_g is the group velocity at the resonant frequency of the dipole ω_d. The formula indicates that the largest F_{PCW} is achieved when the wavepacket group velocity reaches zero. Thus, the design of a PCW efficiently coupled with a single emitter resonant at ω_d is equivalent to engineering a PCW dispersion law to meet the requirement $d\omega/dk|_{\omega=\omega_d} = 0$. Numerical methods for calculation of the dispersion structure of a PCW are well known and straightforward [28] and can be easily applied to a PCW with a defined geometry. However, there exists no recipe for how to estimate geometric parameters of a PCW exhibiting a high Purcell factor at a wavelength of interest. We devise heuristic expressions linking the target wavelength and the parameters of a triangular PCW that stem from simple optical effects occurring inside a photonic crystal.

III. PCW-PURCELL-FACTOR HEURISTICS

The geometry of a unit cell of the PCW considered is shown in Fig. 3. The corresponding parameters are the

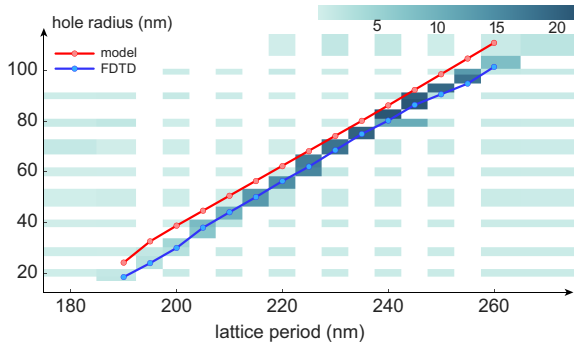

FIG. 2. The set of configurations in (a, r)-parameter space corresponding to a peak F_{PCW} at 925 nm. The 2D heatmap represents the F_{PCW} values experienced by the emitter in a PCW with given a and r. The a and r values are unevenly distributed for time-saving purposes. We added extra points in the maximal F_{PCW} region. The white tiles represent the points that were not computed. The blue curve connects the maximal F_{PCW} values calculated numerically by 3D FDTD simulation. The red curve contains values estimated by the proposed heuristic theoretical approach.

lattice period a, the hole radius r, the PC hole-pattern angle θ_l, the membrane height h, and the membrane refractive index n. The inset in Fig. 1 illustrates a typical dispersion structure of a PCW. The geometric parameters for this example were taken as follows: pattern angle $\theta_l = 60°$, period $a = 0.238$ μm, hole radius $r = 0.08$ μm, and membrane thickness $h = 0.16$ μm. These values were chosen to put the Purcell-factor F_{PCW} peak at 925 nm. A natural question arises of whether this configuration is unique. It turns out that the answer is negative.

We performed an extensive numerical analysis of the Purcell enhancement happening in different PCW configurations; the results are presented in Fig. 2. The 3D FDTD simulation was performed with the Ansys LUMERICAL FDTD package; the details of the simulation are given in Appendix D. We observed a continuous set of configurations of a triangular PCW with the same lattice angle corresponding to a peak value of F_{PCW} at a target wavelength. We consider the parameters that reveal the Purcell-factor peak at a given wavelength λ. We assume that the relation between them can be written in the form $a = c_1(a, r, \lambda, n) + c_2(a, r, \lambda, n, h)r$, where the coefficients c_1 and c_2 are weakly dependent on a and r. The $a(r)$ dependence is finely approximated by a linear function in the region where F_{PCW} reaches its highest values.

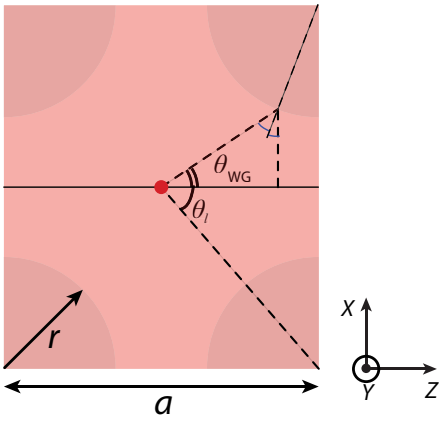

FIG. 3. Geometry of the unit cell of a PCW considered in the model.

In the following subsections we provide a heuristic theoretical description for the origins of such a dependence and the values of c_1 and c_2.

A. The slope coefficient c_2

The probability of single-photon emission to a PCW guided mode is, in general, given by

$$\beta = \frac{\Gamma_{\mathrm{PCW}}}{\Gamma_{\mathrm{PCW}} + \Gamma_r + \Gamma_{\mathrm{NR}}}, \tag{2}$$

where Γ_{PCW} and Γ_r are the rates of emission to a PCW guided mode and PCW nonguided modes, respectively, and Γ_{NR} is the nonradiative-decay rate of the QD. The existence of a PCW mode is a purely interferometric effect; hence, the probability β should be mostly related to the geometry of the photonic crystal. We expect to derive the connection between the geometric parameters that correspond to a configuration of a PCW structure with a maximal Purcell factor at the required wavelength. For this purpose we simplify the system by omitting the nonradiative-decay rate Γ_{NR} because the numerical model does not account for it. Next we identify the main radiative-decay channel—a vertical Fabry-Perot (FP) cavity. We can now decompose the PCW as a combination of two structures: a vertical Fabry-Perot cavity and a 2D (of infinite height) photonic crystal waveguide (see Fig. 4). This viewpoint justifies a much-simpler formula for the probability of emission into either the FP cavity or the PCW,

$$\beta = F/(1 + F), \tag{3}$$

since the subsystems are considered independently of one another. The Purcell factor F can be easily estimated for both the FP cavity and the PCW. We link β_{FP} and β_{PCW} by analyzing the dipole radiation inside the PCW structure and thus end up with a relation between PCW geometric parameters and the target wavelength at which F_{PCW} should be maximized.

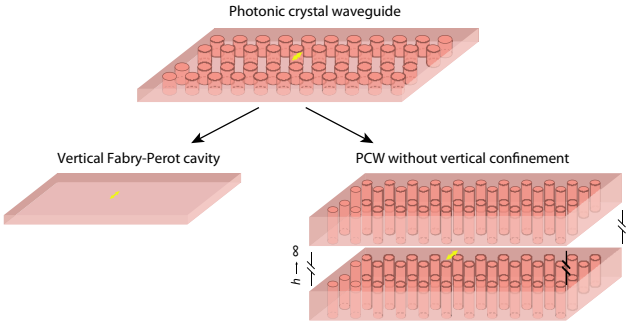

FIG. 4. Splitting the PCW (center) into two structures: vertical Fabry-Perot cavity (left) and 2D PCW (right). The simplified structures allow derivation of the connection between PCW parameters and Purcell enhancement.

We derive the following equation:

$$\left(1-\frac{F_{\mathrm{FP}}}{1+F_{\mathrm{FP}}}\right)\frac{\int_{\pi/2-\theta_{\mathrm{WG}}}^{\pi/2+\theta_{\mathrm{WG}}}\sin^3\theta d\theta}{\int_0^{\pi}\sin^3\theta d\theta}\frac{1}{\pi}\int_0^{\pi}\sin\phi d\phi = \frac{F_{\mathrm{PCW}}(a,r)}{1+F_{\mathrm{PCW}}(a,r)}, \tag{4}$$

where β_{PCW} and β_{FP} are the probabilities of a dipole emitting light into a 2D-PCW guided mode and into a vertical-FP-cavity mode, respectively. Because the FP-cavity mode is of infinite width, the eigenmode wavevector is perpendicular to the cavity plane. In this case $1-\beta_{\mathrm{FP}}$ is the probability of emitting the photon not into the cavity eigenmode, regulated by the dipole-emission pattern. The term $1/\pi\int_0^{\pi}\sin\phi d\phi = 0.637$ corresponds to the fraction of intensity emitted parallel to the FP-cavity surface. We multiply the left side of Eq. (4) by a fraction of the dipole emission into an effective PCW guided-mode angle θ_{WG}, which is defined later. The term $\sin^3\theta d\theta$ includes contributions from the dipole-radiation pattern $\sin^2\theta$ and transition to the spherical coordinate system $\sin\theta$. One can see that the right-hand side of Eq. (4) describes the same fraction of radiation, because the 2D PCW has an eigenmode with the wavevector in the plane perpendicular to the holes and the angular spectrum spanning the PCW guided-mode angle θ_{WG}.

Now we are left with three values, F_{FP}, F_{PCW}, and θ_{WG}, that we need to express using the PCW geometric parameters.

We start with evaluation of F_{FP}. We treat the vertical FP cavity as an independent subsystem and use Eq. (3) to estimate the fraction of light emitted by the dipole into the cavity mode. The resonance frequency $\omega_1 = \pi c/nh$ and the linewidth $dw = c(1-R)/n\sqrt{R}h$ for the first eigenmode of this FP resonator are expressed with use of the PC thickness h and the refractive index of the material n. The Fresnel law yields the reflection coefficient $R = (n-1)^2/(n+1)^2$ for light incident normally on the PC surfaces. The FP Purcell factor is given by

$$F_{\mathrm{FP}} = \frac{3Q(\lambda/n)^3}{4\pi^2 V_{\mathrm{eff}}^{\mathrm{FP}}}\times\frac{d\omega^2}{4(\omega-\omega_1)^2+d\omega^2}. \tag{5}$$

The effective mode volume is given by $V_{\mathrm{eff}} = \int_V \epsilon E^2 dV/\max_V(\epsilon E^2)$ [29], where the integration is performed over a single unit cell for periodic structures (for example PCWs) and over the whole possible volume for nonperiodic structures (the period equals infinity). For such a configuration the effective mode volume can be estimated as $V_{\mathrm{eff}}^{\mathrm{FP}} = \frac{2}{3}h^3$ (see Appendix B). F_{FP} of the vertical mode resonator is then approximately 0.64 if we set $\lambda = 925$ nm and $n_{\mathrm{GaAs}}(\lambda = 925\ \mathrm{nm}) = 3.46$.

Next we need to express $F_{\mathrm{PCW}}(a,r)$. We consider a unit cell as a rectangle with four quarter circles (see Fig. 3). We consider a PCW dispersion curve with $d\omega/dk|_{\omega=\omega_d} = 0$ and focus on the system's behavior at a frequency ω slightly less than ω_d. We assume that the mode volume of light modes at frequencies $\omega < \omega_d$ is roughly the same as at the resonance frequency ω_d, because the slight change of the light's frequency should not affect the mode volume. Light at frequency ω can populate only the modes satisfying the free-space dispersion relation $\omega = ck/n(\omega)$. The effective mode volume for the light modes with the free-space dispersion relation is defined by

$$V_{\mathrm{eff}}^{\mathrm{PCW}} = \frac{\int_V I dV}{\max_V I} = \frac{\langle I\rangle V}{I_0}, \tag{6}$$

where I denotes the radiation intensity inside the unit cell.

Figure 5 illustrates the setting that we use to estimate $V_{\mathrm{eff}}^{\mathrm{PCW}}$. We study a unit cell of the PCW that is located far from the dipole emitter since we are interested in the PCW guided-mode volume, which does not depend on the dipole location. In this case the near-field effects of the dipole emission within the structure may be safely omitted and the $I(z) = \mathrm{const}/z^2$ scaling of emitted intensity can be used. Let the unit cell "entrance" coordinate along the propagation axis be z_0 (see Fig. 5). The average intensity in the unit cell is then

$$\langle I(z)\rangle = \frac{1}{a}\int_{z_0}^{z_0+a}\frac{\mathrm{const}}{z^2}dz = \frac{\mathrm{const}}{(\langle z\rangle+z_0)^2}, \tag{7}$$

where $\langle z\rangle$ is the coordinate of a point inside the cell with the average intensity value ($0 < \langle z\rangle < a$).

If we consider the stationary PCW eigenmode, we must set $z_0 \to \infty$, because the ideal mode profile is formed at the furthest point from the dipole. In this case one can easily see from Eq. (7) that $\langle z\rangle = a/2$ (yellow dot in Fig. 5). This result implies that we need to consider $\langle I\rangle$ as the intensity at the $\langle z\rangle$ coordinate, taking into account diffraction effects at the unit cell "entrance." We need to calculate

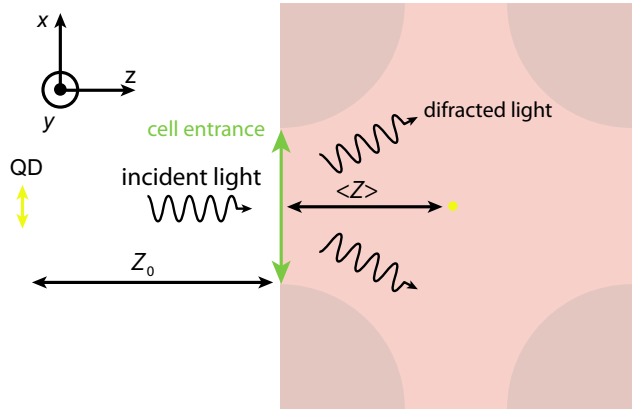

FIG. 5. Description of the PCW effective mode volume using the diffraction effects on the unit-cell entrance. z_0 is the distance between the emitter (QD) and the unit cell.

the number of Fresnel zones at the $\langle z \rangle$ coordinate in the center of the waveguide, taking into account that the sizes of the structure are comparable with the wavelength and that light propagates mainly in the material with refractive index n. In this case the estimated number of Fresnel zones (we assume that the unit cell is located far from the dipole, so the light propagates almost parallel to the waveguide axis) can be found from the following equation:

$$m : (a\sqrt{3}/2 - r)^2 = m(\lambda/n)\langle z \rangle + m^2(\lambda/n)^2/4. \tag{8}$$

We get $m \approx 0.95$, which means that the Fresnel approximation is valid [30]. Since the unit-cell-entrance cross section is rectangular, we calculate the parameters of the Cornu spiral as

$$\begin{aligned} u &= \sqrt{2m}, \\ c(u) &= \textstyle\int_0^u \cos(\frac{\pi}{2}\tau^2)d\tau, \\ s(u) &= \textstyle\int_0^u \sin(\frac{\pi}{2}\tau^2)d\tau. \end{aligned} \tag{9}$$

The coefficients $c(u)$ and $s(u)$ allow one to evaluate the required ratio

$$\frac{\langle I \rangle}{I_0} = \frac{c(w)^2 + s(w)^2}{c(\infty)^2 + s(\infty)^2}. \tag{10}$$

In this case the effective mode area per unit cell can be estimated as $S_{\text{eff}}^{\text{PCW}} = \langle I \rangle/(I_0)S_{\text{cell}}$ in the plane perpendicular to the PCW holes. The effective height of the mode can be estimated as $l_\phi \approx a$ as for the vertical Fabry-Perot cavity. Then the effective mode volume is given by $V_{\text{eff}}^{\text{PCW}} = \langle I \rangle/I_0 a S_{\text{cell}}$, where V is the geometric volume of the unit cell. $V_{\text{eff}}^{\text{PCW}}$ approximately equals 22×10^6 nm^3, which is roughly 1.3 times larger than $(\lambda/n)^3$.

Lastly we need to derive a relation between θ_{WG} and the parameters of the PCW. The expression connecting the geometric parameters of the crystal to the value of θ_{WG} is defined by the crystal configuration. The θ_{WG} geometric definition is illustrated in Fig. 3, which is valid for a triangular PC with $\theta_l = 60°$. We get the formula for θ_{WG} assuming it to be the marginal angle of incidence on the hole border for which the reflected beam still has a nonzero wavevector component parallel to the waveguide axis. In a triangular lattice it is implicitly related to the period a and the hole radius r (see Appendix A):

$$\frac{a}{r} = \frac{\cos(\pi/4 - \theta_{\text{WG}}/2) - \tan\theta_{\text{WG}} \sin(\pi/4 - \theta_{\text{WG}}/2)}{\tan\theta_l/2 - \tan\theta_{\text{WG}}/2}, \tag{11}$$

where θ_l is the lattice angle. θ_{WG} may be interpreted as the angular width of the PCW guided mode (see Appendix E).

Now we have all the ingredients needed to calculate the coefficient c_2. We substitute F_{PCW} and F_{FP} into Eq. (4) and solve it for θ_{WG}. Once θ_{WG} is known, Eq. (11) allows us to calculate $a/r = c_2$. Explicit formulas and a numerical-calculation algorithm are provided in Appendix C.

B. The constant coefficient c_1

We are now interested in deriving an equation for the constant coefficient c_1. Its impact is most significant when $r \to 0$. In this limit we can consider the system as a set of reflective planes (see Fig. 6), where by a "reflective plane" we mean a cross section of the PC structure passing through a row of holes. F_{PCW} reaches its peak value when the emission towards any direction other than the PCW axis is suppressed. We first define the angle α_{av}, which corresponds to the average direction of dipole emission as follows:

$$\int_0^{\pi/2} \sin^3\theta \cos\alpha_{\text{av}} d\theta = \int_0^{\pi/2} \sin^3\theta \cos\theta d\theta. \tag{12}$$

The term $\sin^2\theta$ describes the dipole-radiation pattern. A $\sin\theta$ term arises from the transition to a spherical coordinate system. Lastly the $\cos\theta$ term on the right-hand side implies that we are interested in a projection on the vertical axis, because we are looking for the destructive-interference condition for light waves propagating perpendicular to the waveguide axis.

Let us write down a set of Bragg conditions for destructive interference at the set of reflective planes. We take into account only two types of reflective plane: reflective planes parallel to the waveguide and reflective planes tilted as shown in Fig. 6. These two sets of planes share similar properties: the distance between the holes along these planes is minimal over all other possible planes and equals the crystal lattice parameter a. We do not take into account the interference effects happening at every other possible set of planes due to the increasing distance between the circles forming these planes and thus the necessity to take

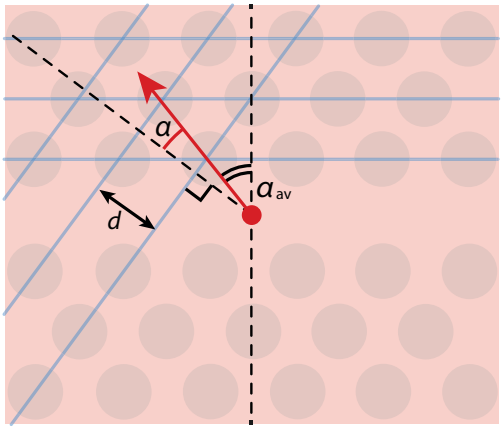

FIG. 6. Geometry of the effective reflective planes used to calculate the constant coefficient c_1. Blue lines indicate which hole groups form reflective planes.

diffraction effects into consideration. For the tilted planes, the Bragg condition is

$$\begin{aligned} 2dn\cos(\alpha) &= \lambda, \\ \alpha &= \theta_l - \alpha_{\text{av}}, \\ d &= a_{\text{slop}}\sin(\theta_l). \end{aligned} \tag{13}$$

The PC period satisfying this condition is denoted a_{slop}.

The Bragg condition for the parallel planes is

$$2\frac{a_{\text{par}}\tan\theta_l}{2} n\cos\alpha_{\text{av}} = \lambda, \tag{14}$$

where a_{par} is the PC period that satisfies the second Bragg condition. Finally, we estimate the fractions of radiation that preferentially interfere in the sloped and parallel sets of planes. These fractions are obtained with use of the dipole-radiation pattern:

$$\begin{aligned} \eta_{\text{slop}} &= \frac{\int_{\pi/2-\theta_l}^{\pi/2}\sin^3\theta\cos\theta d\theta}{\int_0^{\pi/2}\sin^3\theta\cos\theta d\theta}, \\ \eta_{\text{par}} &= \frac{\int_0^{\pi/2-\theta_l}\sin^3\theta\cos\theta d\theta}{\int_0^{\pi/2}\sin^3\theta\cos\theta d\theta}. \end{aligned} \tag{15}$$

Taking these fractions into account, we can now express the total constant coefficient through a and r as a weighted average value:

$$c_1 = \eta_{\text{par}}a_{\text{par}} + \eta_{\text{slop}}a_{\text{slop}}. \tag{16}$$

C. Comparison of the heuristic model and FDTD simulation

The final model $a = c_1 + c_2 r$ was tested alongside FDTD simulations. Three elements of the parameter space of the PCW configuration $\{a, r, h, n, \lambda\}$ were fixed and we maximized the Purcell enhancement using the other two. Figure 7 illustrates the outputs of the proposed heuristic model side-by-side with the best configuration that was devised through FDTD simulation. The plots in Figs. 7 show the results obtained when different subspaces of variables are selected. The results in Figs. 7(a), 7(c), and 7(d) calculated with the heuristic model reproduce the same trend as that visible in FDTD simulations. We see a systematic bias of the heuristic model to output larger values of the hole radius r. We think that this bias may be eliminated by a more-careful account of the infinite range of Bragg conditions, which affect the constant c_1. The graph in Fig. 7(b) may indicate that the Fabry-Perot approximation of the vertical-resonator decay channel is not very accurate.

IV. IMPROVEMENT OF THE PCW ROBUSTNESS WITH REGARD TO FABRICATION IMPERFECTIONS USING COMPOSITE PCW STRUCTURES

The proposed heuristic theory can be applied for the design of new PC structures that potentially might reveal interesting phenomena. We demonstrate the increase of robustness of the Purcell enhancement with regard to random perturbations of the hole radii. One can note from Fig. 2 that different combinations of PC period a and hole radius r lead to emission rate enhancement in the PCW at the same wavelength. We conjecture that if two PCWs with different lattice periods a_1 and a_2 and hole radii r_1 and r_2, respectively, correspond to the same design frequency ω_d, then the compound crystal will also enhance the emission at frequency ω_d (see Fig. 8).

We suggest that the compound PCW in the center of Fig. 8 is more robust with regard to fabrication imperfections than a standard one. If we introduce slight random deviations to the values of the radius r, the F_{PCW} spectral curve shifts away from the target frequency and the coupling of the dipole radiation to the PCW mode decreases substantially. We do not take into account random shifts of the PCW period a because a is several times larger than the deviation due to manufacturing imprecision introduced in state-of-the-art fabrication lines [31]. It is also worth noting that a systematic bias of a and r is easily accounted for by our theoretical description. If the bias in each of the parameters a and r can be determined experimentally, the other parameter can be adjusted accordingly with use of the formulas for c_1 and c_2. The idea behind increased robustness with regard to fabrication errors relies on simple reasoning. β becomes greater than 0.9 even at moderate $F_{\text{PCW}} \approx 10$ or greater, which can already be considered as good coupling of the emitter radiation to the PCW mode. The F_{PCW} spectral dependence in a standard PCW structure is typically very narrow. Our goal is to design the PCW structure so as to make $F_{\text{PCW}}(\lambda)$ wider at the expense of

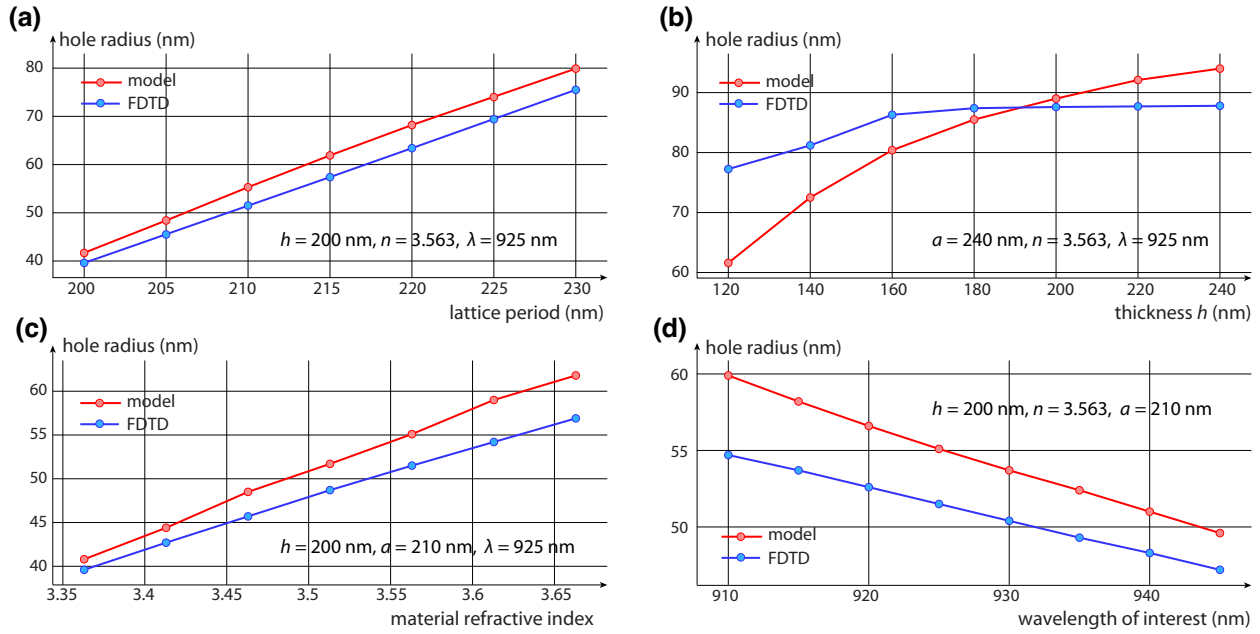

FIG. 7. Comparative analysis of the output of the proposed heuristic model and the FDTD-simulation results. Each point corresponds to the configuration that exhibits maximal Purcell enhancement.

the F_{PCW} peak value becoming lower but still sufficient for good coupling.

We prove our point by performing numerical simulations using the software package LUMERICAL. The model describes a composite PCW structure comprising two half-crystals with different periods and hole radii. Each half is designed to provide maximal Purcell enhancement at wavelength $\lambda = 925$ nm. We add random additive δr_i sampled from the $[-10, 10]$ nm interval to the radius of each hole in the numerical PCW model and perform 100 unique simulation runs. Details of the numerical simulation are provided in Appendix D. Figure 9 illustrates the results of the simulation. Compound PCW structures with more-distinct parameters for each half demonstrate advantageous robustness. The spectral width of the Purcell-enhancement curve becomes greater and a large value of F_{PCW} at the target wavelength occurs more frequently. To quantify the performance we introduce an average Purcell-enhancement factor $\tilde{F}_{\mathrm{PCW}}$ and a probability of Purcell enhancement p. The target wavelength lies within the width at half maximum of the Purcell-enhancement curve in $p \times 100$ instances of simulations, where p is the probability of Purcell enhancement. $\tilde{F}_{\mathrm{PCW}}$ is the mean value of F_{PCW} in these instances. The best compound crystal with periods $a_1 = 225$ nm and $a_2 = 240$ nm and target wavelength $\lambda_1 = \lambda_2 = 925$ nm demonstrates Purcell enhancement $F_{\mathrm{PCW}} > 5$ in 47% of simulated instances. This compound-crystal configuration demonstrates better performance (Fig. 9, left column, central panel) with simulated fabrication defects compared with the standard PCW with identical halves (Fig. 9 top row, left panel).

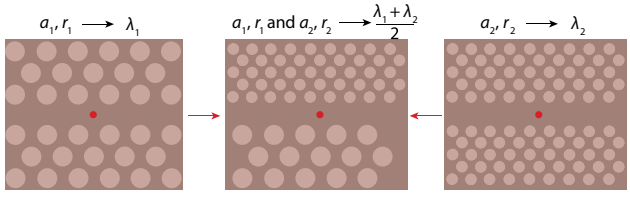

FIG. 8. Compound PCW composed of two half-PCWs, designed to exhibit a peak value of F_{PCW} at λ_1 and λ_2, which satisfy the condition $\lambda_1 + \lambda_2 = 2\lambda_0$.

Another option is to consider a compound PCW composed of two parts designed to exhibit a maximal F_{PCW} value at different wavelengths λ_1 and λ_2. Here the question arises of at which wavelength the maximal F_{PCW} of a compound crystal will be observed. The answer turns out to be simple: if the parts of the PCW reveal the peak F_{PCW} value at wavelengths λ_1 and λ_2, respectively, then the compound PCW reveals the peak at $(\lambda_1 + \lambda_2)/2$. One can easily prove this statement by taking into account that there are two different reflective-plane systems (under an approximation of a small hole radius r, see Fig. 6), and to prevent light from propagation in a direction perpendicular to the waveguide axis, the effective distance between each plane must be equal to $\lambda/2$, meaning that the total effective distance between the planes on both sides of the emitter should be $(\lambda_1 + \lambda_2)/2$.

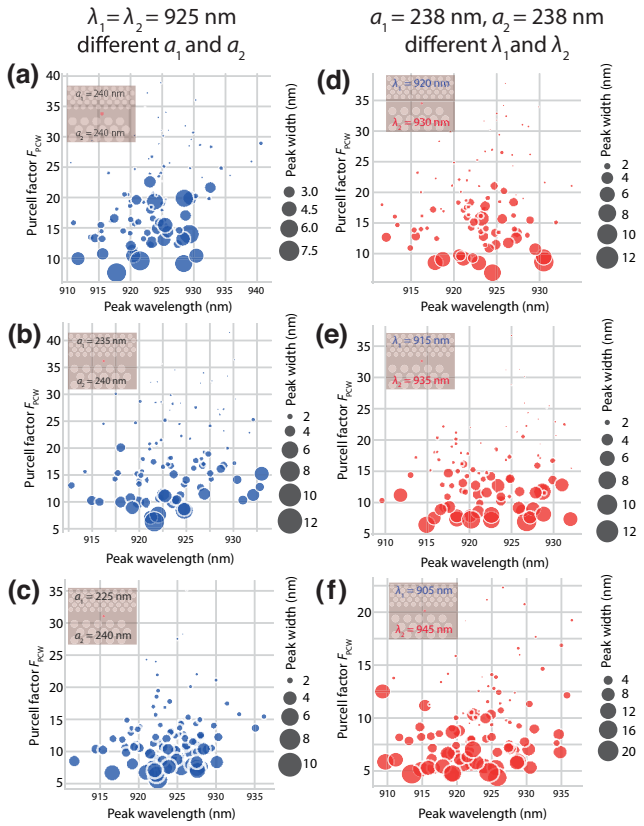

FIG. 9. Summarized results of the simulations of F_{PCW} spectral curves for the compound crystals. Each panel depicts the F_{PCW} peak values and full widths at half maximum for each of the 100 curves computed for compound PCWs with added randomized hole-radius error. The left column shows the results for compound structures composed of two halves of PCWs optimized for identical peak F_{PCW} wavelength $\lambda_0 = 925$ nm. The right column shows the results for compound structures composed of two halves of PCWs optimized for different λ_1 and λ_2 satisfying $\lambda_1 + \lambda_2 = 2\lambda_0$. The insets illustrate the set of variable parameters used.

The numerical results for this composition method are also obtained with use of 100 FDTD simulations similar to those used previously. The results are shown in the right column in Fig. 9. The conclusion for this case is as follows: the greater is the difference between the wavelengths of both parts of a compound PCW, the less is the maximal value and the greater is the Δ_{FWHM} of the F_{PCW} spectral curve. The periods for both parts can be the same or different, but the radius must be set according to our model, so that each part of the PCW shows a peak at the required wavelength.

Results of the simulation of the Purcell-factor spectral curve in the combined crystals with randomized radius error $\delta r \in [-10, 10]$ nm are summarized in Table I. We observe the tendency of the probability p to increase when the two halves of the PCW are designed with largely different parameters.

TABLE I. Summary of the combined crystal performance according to numerical simulations. The mean Δ_{FWHM} and mean F_{PCW} values indicate the Purcell-factor Δ_{FWHM} and maximal value averaged over 100 simulation runs. The errors are standard deviations over 100 simulation runs. The PCW had 15 holes in the propagation direction and 11 holes in the perpendicular direction. Δp was estimated according to the binomial distribution $\Delta p = \sqrt{100p(1-p)}/100$.

Configuration	$\overline{F_{PCW}}$ ($\lambda = 925$ nm)	$p \pm \Delta p$	Δ_{FWHM} (nm)	$\overline{F_{PCW}}$ (λ_{peak})	$\overline{\lambda_{peak}}$
$\lambda_1 = \lambda_2 = 925$ nm and $a_1 = a_2 = 240$ nm	7.6 ± 8.5	0.29 ± 0.05	3.1 ± 1.7	20.8 ± 7.3	923.9 ± 5.6
$\lambda_1 = \lambda_2 = 925$ nm and $a_1 = 235$ nm, $a_2 = 240$ nm	5.2 ± 4.9	0.23 ± 0.04	3.3 ± 1.9	19.5 ± 8.3	924 ± 4.3
$\lambda_1 = \lambda_2 = 925$ nm and $a_1 = 225$ nm, $a_2 = 240$ nm	5.2 ± 4.6	0.47 ± 0.05	4.5 ± 2	12.5 ± 5	924.2 ± 4.1
$\lambda_1 = 920$ nm, $\lambda_2 = 930$ nm and $a_1 = a_2 = 240$ nm	6.1 ± 7.3	0.28 ± 0.04	3.4 ± 2.1	18.8 ± 7.2	923 ± 4.5
$\lambda_1 = 915$ nm, $\lambda_2 = 935$ nm and $a_1 = a_2 = 240$ nm	4.9 ± 6.2	0.26 ± 0.04	4 ± 2.4	15.8 ± 6.5	922.7 ± 5.1
$\lambda_1 = 905$ nm, $\lambda_2 = 945$ nm and $a_1 = a_2 = 240$ nm	3.7 ± 3.1	0.46 ± 0.05	7.8 ± 5.3	9.7 ± 4	923.1 ± 6

V. DISCUSSION AND CONCLUSION

We have established a mathematical connection between geometric parameters of a PCW structure and a Purcell-enhancement factor at a specific wavelength. Compound PCW structures, which are predicted to provide maximal enhancement at the target wavelength, exhibit stronger robustness with regard to the random hole-radius deviation compared with standard PCW structures. We attribute the observed effect to the broken symmetry of the crystal. The improvement manifests itself in higher probability of a dipole emitter being efficiently coupled to a PCW mode and the higher average Purcell-enhancement factor $\tilde{F}_{\mathrm{PCW}}$. The $\tilde{F}_{\mathrm{PCW}}$ values are around 5, which yields β of approximately 83%. Although such coupling-efficiency values cannot be considered as satisfactory for the most-demanding applications such as fault-tolerant linear optical quantum computing [32,33], they can nevertheless enable near-term experiments with multiple single-photon sources on an integrated platform. The result does not demonstrate an extreme robustness improvement; however, it illustrates the capability of the heuristic model developed to produce PCW configurations exhibiting interesting features.

The robustness features of the demonstrated compound PCW structures have very different roots from those of topological photonic systems [34–37]. Topological robustness exists in very special classes of photonic crystals with dispersion properties satisfying the conditions yielding nontrivial values of topological invariants for the guided modes. Also the robustness of these types of waveguide usually means the survival of the mode whenever perturbations to the structure are introduced. Our approach focuses more on the practical features of the PCWs. i.e., the Purcell enhancement of dipole-emitter radiation. We view robustness as a property of the structure characterizing the stability of the Purcell enhancement at the wavelength of interest.

Our results provide a clear understanding of the interplay of PCW parameters and thus they significantly simplify the initial structure-design procedure. They can also serve to augment sophisticated automated-optimization design routines by narrowing down the parameter space or serving as a quick sanity check avoiding the necessity to run a 3D FDTD simulation. Our heuristic model describes a triangular PCW structure only, but we believe that similar reasoning and mathematical analysis should apply to any other photonic crystal layout.

ACKNOWLEDGMENTS

A.S., I.D., and S.S. acknowledge support by Rosatom in the framework of the Roadmap for Quantum Computing (Contract No. 868-1.3-15/15-2021 dated October 5, 2021, and Contract No. P2154 dated November 24, 2021). S.K. is supported by the Ministry of Science and Higher Education of the Russian Federation on the basis of the Federal State Autonomous Educational Institution of Higher Education South Ural State University (National Research University) (Agreement No. 075-15-2022-1116).

APPENDIX A: THE $\frac{a}{r}$ FORMULA

The idea underlying the derivation of the formula for θ_{WG} is as follows: θ_{WG} is the angle between the waveguide's axis and a beam that is reflected without obtaining a component parallel to the waveguide's axis [see Fig. 1(d)]. Then we can use simple geometric relations to get

$$\tan\theta_{\mathrm{WG}} = \frac{AB}{BC} = \frac{a\tan\theta_l/2 - r\cos\alpha}{a/2 - r\sin\alpha} \tag{A1}$$

and $\alpha = \pi/4 - \theta_{\mathrm{WG}}/2$. Once we combine these relations, we get the equation

$$\tan\theta_{\mathrm{WG}} = \frac{a\tan\theta_l/2 - r\cos(\pi/4 - \theta_{\mathrm{WG}}/2)}{a/2 - r\sin(\pi/4 - \theta_{\mathrm{WG}}/2)}, \tag{A2}$$

which yields the formula in the form of Eq. (11):

$$\frac{a}{r} = \frac{\tan\theta_{\mathrm{WG}}\sin(\pi/4 - \theta_{\mathrm{WG}}/2) - \cos(\pi/4 - \theta_{\mathrm{WG}}/2)}{\tan\theta_{\mathrm{WG}}/2 - \tan\theta_l/2}. \tag{A3}$$

APPENDIX B: ESTIMATED VALUE OF THE EFFECTIVE MODE VOLUME FOR A FLAT-SURFACE FABRY-PEROT RESONATOR

We use a simple relation to estimate an effective mode volume $V_{\mathrm{eff}} = hS_{\mathrm{eff}}$ of the Fabry-Perot resonator, comprising the top and bottom surfaces of the PCW membrane (see Fig. 4). We take into account the angular structure of the dipole radiation that has the form of the product of two functions $f(\theta)f(\phi)$, where θ and ϕ are the polar and azimuthal angles, respectively. θ is counted from the dipole axis. On that basis, we can estimate the effective mode area S_{eff} as the product of the effective mode lengths in both polar and azimuthal directions. The effective mode length for each direction can be derived as

$$l_{\mathrm{eff}} = \frac{\int_L Idl}{I_{\max}}. \tag{B1}$$

The intensity is inversely proportional to the distance between the source and the observation point, and hence we have $I_{\max} \sim 1/(h/2)^2$ and $I \sim 1/AC^2$. We use the geometric relations $AC = h/(2\sin\theta)$, $DC = h/2\theta$, and $dl = d(DC) = \frac{h/2}{\sin^2\theta}d\theta$ and substitute them into Eq. (B1). We also need to account for the dipole-radiation angular dependence $\sin^2\theta$ and the term $\sin\theta$ or $\sin\phi$ corresponding to projection on the z axis, because we are considering only light modes propagating perpendicular to the PCW membrane. The dependence on the azimuthal angle ϕ

accumulates only a single $\sin\phi$ term due to the absence of dependency on ϕ in the dipole-emission pattern. The final integrals for both effective lengths are given by

$$l_\theta \sim \frac{1}{I_{\max}} \int_0^\pi \frac{\sin^3(\theta)}{h/2} d\theta,$$
$$l_\phi \sim \frac{1}{I_{\max}} \int_0^\pi \frac{\sin(\phi) d\phi}{h/2}. \tag{B2}$$

The integration yields the effective lengths $l_\theta \approx \frac{2}{3}h$ and $l_\phi \approx h$. The total effective mode volume is then given by $V_{\text{eff}} = h \times \frac{2}{3}h \times h = \frac{2}{3}h^3$.

APPENDIX C: THE CALCULATION ALGORITHM FOR *r*

One can use the following procedure to calculate the hole radius r given the parameters h, n, λ_d, and a:

(1) Set an initial guess r_0 for the radius for the given a; it should be relatively close to the exact value.
(2) Calculate F_{FP} using Eq. (5).
(3) Calculate F_{PCW} using Eqs. (6)–(10) and use r_0 defined in step 1. After calculating the PCW mode volume, substitute it into Eq. (1).
(4) Calculate the slope coefficient c_2 for the given a using Eq. (11).
(5) Calculate the coefficient c_1 using Eqs. (13)–(16).
(6) The exact radius for the model can now be estimated as $r = (a - c_1)/c_2$.
(7) Repeat all the steps using r as the new initial value. This should be done until the initial value of the radius set in step 1 equals the exact value, which was obtained in step 6.

Such a procedure is necessary due to the explicit dependence $r(a)$, and it is the easiest way to obtain the result.

APPENDIX D: DETAILS OF THE FDTD SIMULATION

The PC-waveguide dispersion was calculated for the ordinary PCW (without disorder) in the following way. The simulation uses Bloch boundary conditions in the direction perpendicular to the waveguide axis. We use a dipole cloud as a source of radiation that excites multiple possible modes in the system. The randomly positioned electric field monitors record the local field amplitude versus the simulation time. The recorded traces are then decomposed as an infinite sum of exponentially decaying harmonic functions. Frequencies with the least decay rate are considered to be eigenfrequencies corresponding to a given wavevector modulus k, which is used to specify Bloch boundary conditions. The size of the simulation region was $a \times a\sqrt{3} \times 3\ \mu\text{m}^3$ for the triangular lattice, where the first two parameters determine the unit cell and the third parameter is the size along the axis, perpendicular to the PCW plane.

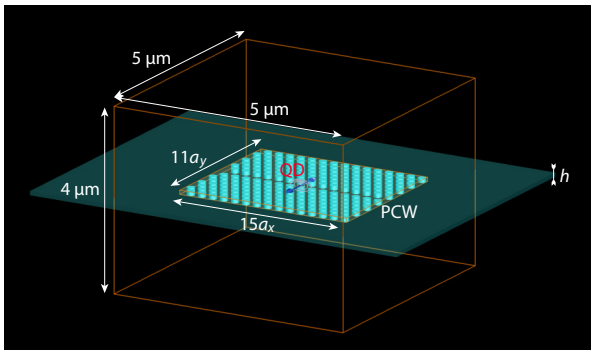

FIG. 10. Simulation setup for numerical solution of Maxwell equations with LUMERICAL FDTD.

We used a numerical model of a PC waveguide for comparison with the predictions of our heuristic model. We set up the simulation of a PCW structure in LUMERICAL FDTD. We set the transverse dimensions of a GaAs membrane to be larger than the simulation region to avoid internal reflections inside the crystal. We used perfectly-matched-layer boundary conditions along the waveguide axis as well as above and below the membrane. We did not set any specific Dirichlet boundary conditions [28], because we are not focused on precise calculation of the field distribution in the PCW structure. The perfectly-matched-layer boundary conditions must not overlay the features of the PCW so as to exclude numerical artifacts. The disordered crystal was simulated in the same way, because we are interested in the realistic finite structure.

The Purcell factor F_{PCW} at the wavelength of interest was estimated with use of the built-in function in the software package LUMERICAL FDTD. This function returns the power that is emitted in the structure divided by the power radiated in the homogeneous medium. One can see that this is analogous to calculating the Green's function tensor and the local density of states.

The example of the Purcell-factor spectral dependence is illustrated in Fig. 11. This simulation was done with a simulation domain of size $5 \times 5 \times 4\ \mu\text{m}^3$ with a mesh size of 0.04 μm. An additional mesh with a size of 0.001 μm was applied to the photonic crystal (see Fig. 10).

APPENDIX E: ESTIMATED EIGENMODE WIDTH OF THE PCW

We provide an alternative estimation the effective mode width of the photonic crystal waveguide. First we find the average refractive index of the unit cell in Fig. 3:

$$\bar{n}_{\text{core}} = \frac{\pi r^2}{a^2\sqrt{3}} + n\left(1 - \frac{\pi r^2}{a^2\sqrt{3}}\right), \tag{E1}$$

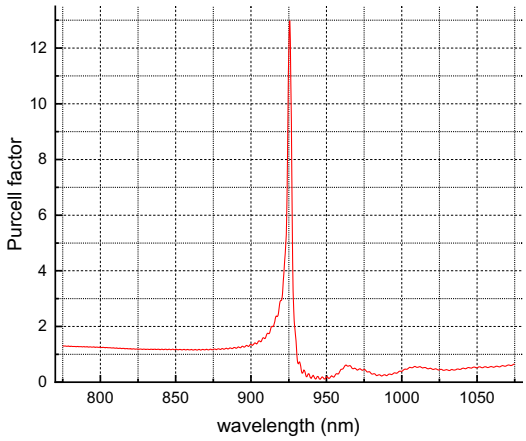

FIG. 11. Example of the numerically computed Purcell-factor spectral dependence for a given crystal configuration.

where n is the refractive index of the PCW material with air holes. We also find the average refractive index of the unit cell adjacent to the cell of the PCW in Fig. 3. Such cells contain an additional hole in the center.

$$\overline{n}_{\text{clad}} = \frac{2\pi r^2}{a^2\sqrt{3}} + n\left(1 - \frac{2\pi r^2}{a^2\sqrt{3}}\right). \tag{E2}$$

Next we find the eigenmode of the 2D waveguide containing the core, which has width $a\sqrt{3}$ and refractive index $\overline{n}_{\text{core}}$, and the cladding with refractive index $\overline{n}_{\text{clad}}$. After substituting the expressions for the fields,

$$E_y(x) = E_0 e^{i\beta z - i\omega t}, \quad H_z(x) = H_0 e^{i\beta z - i\omega t}, \tag{E3}$$

where β is the propagation constant, into the wave equation, we obtain the following relation, taking into account the border conditions for E and H:

$$\sqrt{\overline{n}_{\text{core}}^2 - \beta^2}\,\tan\left(2\pi/\lambda\sqrt{\overline{n}_{\text{core}}^2 - \beta^2}\,a\sqrt{3}/2\right) = \sqrt{\beta^2 - \overline{n}_{\text{clad}}^2}. \tag{E4}$$

From that equation we find β. Because the solution for E inside the cladding is $E \propto e^{-2\pi\sqrt{\beta^2 - \overline{n}_{\text{clad}}^2}\,x/\lambda}$, we get the effective mode waist:

$$w_{\text{eff}} = a\sqrt{3}/2 + \lambda/\left(2\pi\sqrt{\beta^2 - \overline{n}_{\text{clad}}^2}\right). \tag{E5}$$

We can now use w_{eff} to get a rough estimate of the angular width of the guided mode using the Fourier transform. However, we get values that do not correlate well with our heuristic theory after substitution in Eq. (11).

[1] T. Baba, Slow light in photonic crystals, Nat. Photonics **2**, 465 (2008).

[2] G.-J. Tang, X.-T. He, F.-L. Shi, J.-W. Liu, X.-D. Chen, and J.-W. Dong, Topological photonic crystals: Physics, designs, and applications, Laser Photon. Rev. **16**, 2100300 (2022).

[3] S. Mahmoodian, K. Prindal-Nielsen, I. Sollner, S. Stobbe, and P. Lodahl, Engineering chiral light-matter interaction in photonic crystal waveguides with slow light, Opt. Mater. Express **7**, 43 (2017).

[4] J. Vučković and Y. Yamamoto, Photonic crystal microcavities for cavity quantum electrodynamics with a single quantum dot, Appl. Phys. Lett. **82**, 2374 (2003).

[5] H. Zheng, D. J. Gauthier, and H. U. Baranger, Waveguide-QED-based photonic quantum computation, Phys. Rev. Lett. **111**, 090502 (2013).

[6] A. Goban, C. L. Hung, S. P. Yu, J. D. Hood, J. A. Muniz, J. H. Lee, M. J. Martin, A. C. McClung, K. S. Choi, D. E. Chang, O. Painter, and H. J. Kimble, Atom-light interactions in photonic crystals, Nat. Commun. **5**, 3808 (2014).

[7] R. Uppu, F. T. Pedersen, Y. Wang, C. T. Olesen, C. Papon, X. Zhou, L. Midolo, S. Scholz, A. D. Wieck, A. Ludwig, and P. Lodahl, Scalable integrated single-photon source, Sci. Adv. **6**, eabc8268 (2020).

[8] A. Javadi, I. Söllner, M. Arcari, S. L. Hansen, L. Midolo, S. Mahmoodian, G. Kiršanskė, T. Pregnolato, E. H. Lee, J. D. Song, S. Stobbe, and P. Lodahl, Single-photon non-linear optics with a quantum dot in a waveguide, Nat. Commun. **6**, 8655 (2015).

[9] D. Englund, A. Faraon, B. Zhang, Y. Yamamoto, and J. Vučković, Generation and transfer of single photons on a photonic crystal chip, Opt. Express **15**, 5550 (2007).

[10] X. You *et al.*, Quantum interference between independent solid-state single-photon sources separated by 300 km fiber, arXiv e-prints , arXiv:2106.15545 (2021).

[11] A. W. Elshaari, W. Pernice, K. Srinivasan, O. Benson, and V. Zwiller, Hybrid integrated quantum photonic circuits, Nat. Photonics **14**, 285 (2020).

[12] N. Wu, M. Javanmard, B. Momeni, M. Soltani, A. Adibi, Y. Xu, and R. K. Lee, General methods for designing single-mode planar photonic crystal waveguides in hexagonal lattice structures, Opt. Express **11**, 1371 (2003).

[13] A. Säynätjoki, M. Mulot, J. Ahopelto, and H. Lipsanen, Dispersion engineering of photonic crystal waveguides with ring-shaped holes, Opt. Express **15**, 8323 (2007).

[14] L. H. Frandsen, A. V. Lavrinenko, J. Fage-Pedersen, and P. I. Borel, Photonic crystal waveguides with semi-slow light and tailored dispersion properties, Opt. Express **14**, 9444 (2006).

[15] R. Proietti Zaccaria, P. Verma, S. Kawaguchi, S. Shoji, and S. Kawata, Manipulating full photonic band gaps in two dimensional birefringent photonic crystals, Opt. Express **16**, 14812 (2008).

[16] S. Rawal, R. Sinha, and R. M. de La Rue, Slow light miniature devices with ultra-flattened dispersion in silicon-on-insulator photonic crystal, Opt. Express **17**, 13315 (2009).

[17] M. Ebnali-Heidari, C. Grillet, C. Monat, and B. J. Eggleton, Dispersion engineering of slow light photonic crystal waveguides using microfluidic infiltration, Opt. Express **17**, 1628 (2009).

[18] K. Srinivasan and O. Painter, Fourier space design of high-Q cavities in standard and compressed hexagonal lattice photonic crystals, Opt. Express **11**, 579 (2003).

[19] D. Vercruysse, N. V. Sapra, L. Su, and J. Vuckovic, Dispersion engineering with photonic inverse design, IEEE J. Sel. Top. Quantum Electron. **26**, 2950803 (2020).

[20] R. Matzen, J. S. Jensen, and O. Sigmund, Systematic design of slow-light photonic waveguides, J. Opt. Soc. Am. B Opt. Phys. **28**, 2374 (2011).

[21] F. Wang, J. S. Jensen, J. Mørk, and O. Sigmund, Systematic design of loss-engineered slow-light waveguides, J. Opt. Soc. Am. A **29**, 2657 (2012).

[22] H. Men, K. Y. K. Lee, R. M. Freund, J. Peraire, and S. G. Johnson, Robust topology optimization of three-dimensional photonic-crystal band-gap structures, Opt. Express **22**, 22632 (2014).

[23] A. Adibi, Y. Xu, R. K. Lee, M. Loncar, A. Yariv, and A. Scherer, Role of distributed Bragg reflection in photonic-crystal optical waveguides, Phys. Rev. B **64**, 041102(R) (2001).

[24] K. Srinivasan, P. E. Barclay, and O. Painter, Fabrication-tolerant high quality factor photonic crystal microcavities, Opt. Express **12**, 1458 (2004).

[25] M. Fu, J. Liao, Z. Shao, M. Marko, Y. Zhang, X. Wang, and X. Li, Finely engineered slow light photonic crystal waveguides for efficient wideband wavelength-independent higher-order temporal solitons, Appl. Opt. **55**, 3740 (2016).

[26] M. Minkov and V. Savona, Automated optimization of photonic crystal slab cavities, Sci. Rep. **4**, 5124 (2014).

[27] V. S. C. Manga Rao and S. Hughes, Single quantum-dot Purcell factor and β factor in a photonic crystal waveguide, Phys. Rev. B **75**, 205437 (2007).

[28] A. Javadi, S. Mahmoodian, I. Söllner, and P. Lodahl, Numerical modeling of the coupling efficiency of single quantum emitters in photonic-crystal waveguides, J. Opt. Soc. Am. B **35**, 514 (2018).

[29] S. Hughes, Enhanced single-photon emission from quantum dots in photonic crystal waveguides and nanocavities, Opt. Lett. **29**, 2659 (2004).

[30] M. Born and E. Wolf, *Principles of Optics: Electromagnetic Theory of Propagation, Interference and Diffraction of Light (7th Edition)* (Cambridge University Press, Cambridge, England, 1999), 7th ed.

[31] W. Fan, Z. Hao, Z. Li, Y. Zhao, and Y. Luo, Influence of fabrication error on the characteristics of a 2-D photonic-crystal cavity, J. Lightwave Technol. **28**, 1455 (2010).

[32] S. Bartolucci, P. Birchall, D. Bonneau, H. Cable, M. Gimeno-Segovia, K. Kieling, N. Nickerson, T. Rudolph, and C. Sparrow, Switch networks for photonic fusion-based quantum computing, arXiv e-prints, arXiv:2109.13760 (2021).

[33] S. Omkar, S.-H. Lee, Y. S. Teo, S.-W. Lee, and H. Jeong, All-photonic architecture for scalable quantum computing with Greenberger-Horne-Zeilinger states, PRX Quantum **3**, 030309 (2022).

[34] M. Proctor, P. A. Huidobro, B. Bradlyn, M. B. de Paz, M. G. Vergniory, D. Bercioux, and A. García-Etxarri, Robustness of topological corner modes in photonic crystals, Phys. Rev. Res. **2**, 042038(R) (2020).

[35] H. Yoshimi, T. Yamaguchi, Y. Ota, Y. Arakawa, and S. Iwamoto, Slow light waveguides in topological valley photonic crystals, Opt. Lett. **45**, 2648 (2020).

[36] Z. Qi, G. Hu, C. Deng, H. Sun, Y. Sun, Y. Li, B. Liu, Y. Bai, S. Chen, and Y. Cui, Electrical tunable topological valley photonic crystals for on-chip optical communications in the telecom band, Nanophotonics **11**, 4273 (2022).

[37] Z. Lan, M. L. N. Chen, J. W. You, and W. E. I. Sha, Large-area quantum-spin-hall waveguide states in a three-layer topological photonic crystal heterostructure, Phys. Rev. A **107**, L041501 (2023).